Crossover from the coffee-ring effect to the uniform deposit caused by irreversible cluster-cluster aggregation

A. Crivoi,* X. Zhong, and Fei Duan†

School of Mechanical and Aerospace Engineering, Nanyang Technological University, Singapore 639798

(Received 7 February 2015; revised manuscript received 21 August 2015; published 4 September 2015)

The coffee-ring effect for particle deposition near the three-phase line after drying a pinned sessile colloidal droplet has been suppressed or attenuated in many recent studies. However, there have been few attempts to simulate the mitigation of the effect in the presence of strong particle-particle attraction forces. We develop a three-dimensional stochastic model to investigate the drying process of a pinned colloidal sessile droplet by considering the sticking between particles, which was observed in the experiments. The Monte Carlo simulation results show that by solely promoting the particle-particle attraction in the model, the final deposit shape is transformed from the coffee ring to the uniform film deposition. This phenomenon is modeled using the colloidal aggregation technique and explained by the "Tetris principle," meaning that unevenly shaped or branched particle clusters rapidly build up a sparse structure spanning throughout the entire domain in the drying process. The influence of the controlled parameters is analyzed as well. The simulation is reflected by the drying patterns of the nanofluid droplets through the surfactant control in the experiments.

DOI: 10.1103/PhysRevE.92.032302 PACS number(s): 64.75.Yz, 81.16.Dn, 68.03.Fg, 02.70.Uu

I. INTRODUCTION

Both coffee-ring and uniform depositions can be found as remainders of colloidal droplet evaporation in nature and in industrial applications [1,2]. The switch from a ring pattern to uniform deposition or vice versa has been explored since Deegan *et al.* investigated the coffee-ring effect in the pinned droplet drying [3,4]. The inward Marangoni flow [5] has been found to move the particles at the three-phase line of a sessile droplet toward the centerline and attenuate the coffee-ring effect. Shen *et al.* [6] indicated that faster liquid evaporation in the droplet and slower particle motion toward the droplet periphery could reduce the coffee-ring effect; accordingly, the quicker shrinkage of the liquid-vapor interface would increase the possibility of particle collision and sticking. The cationic surfactant is considered as an ingredient reducing the sticking force among the particles and has been used to enhance the coffee-ring effect [7,8]. The ring-like formation was observed in drying graphite water-based nanofluid droplets with the addition of the cetyltrimethylammonium bromide (CTAB) surfactant, while uniform deposition was found after the droplets without surfactant had fully dried [7]. However, the opposite results have been observed after using another surfactant, sodium dodecyl sulphate (SDS). The uniform deposit of polystyrene particles from droplet evaporation was produced with the addition of SDS [9]. Moreover, Yunker *et al.* stated that using ellipsoidal particles led to the suppression of the coffee-ring effect when the droplets were free from surfactant [10]. Dugyala and Basavaraj discussed that the particle-particle interaction was more important than the particle shape by controlling the pH value of liquids [11]. The experimental investigation showed that the particle-particle attraction force played a major role in the crossover from the coffee-ring deposit to the uniform film [7,8,11].

Complex interplay of different experimental phenomena has motivated extensive modeling works in recent years. Various particle-tracking modeling approaches have been applied, including Kandar-Parisi-Zhang (KPZ) and quenched KPZ (QKPZ) methods [12–15], two-dimensional (2D) diffusion limited cluster aggregation (DLCA) [7,16] and hydrodynamic retardation methods [17], a three-dimensional (3D) analytical flow model [18], the 3D biased random walk (BRW) method [19], and ring-growth models [20]. In the present work, we aim to develop a fully 3D model of the drying pinned sessile droplet with uniformly suspended particles on the basis of our previous work [19], also including now the possibility of irreversible slow particle aggregation into fractal-like clusters [21]. We demonstrate the importance of the interparticle attraction strength and its effect on the finally dried structure morphology. The principle, by which the particle clusters change the deposit shape, is discussed in detail and related to the "Tetris principle" [12,22]. The 3D models of the coffee-ring effect based on the analytical equations of Hu and Larsson [23,24] are used. Experimental deposition in alumina-water nanofluid samples with the addition of surfactant under various concentrations is applied for comparison with the finally dried particle deposits in the simulation.

II. MODEL

The mathematical model was developed from the 3D coffee-ring simulation [19] with the additional use of the BRW approach [25–27] coupled with DLCA mechanics [28], allowing the cluster-cluster aggregation process [29] to occur. The main advancement over the previous study [19] is in the extension of the simulations into the parameter range where cluster-cluster aggregation becomes intensive and suppresses the coffee-ring effect. The model is implemented in a 3D domain with a cubical lattice structure, which mimics the shape of a pinned sessile droplet (see Fig. 1). The initial droplet shape is assumed to be a spherical cap with a contact angle. As the pinned droplet evaporates, the geometrical shape is

*Present address: Rolls-Royce@NTU Corporate Laboratory, 50 Nanyang Avenue, Singapore 639798.

†feiduan@ntu.edu.sg

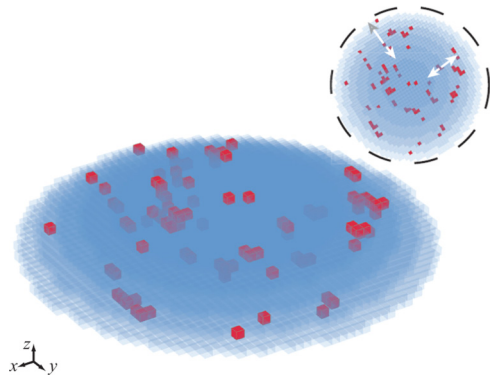

FIG. 1. (Color online) Schematic diagram of the 3D lattice model configuration. The inset shows the top view of the spherical-cap-like domain. The particles in darker cubic shape are shown to be able to aggregate into clusters inside the liquid phase.

assumed to remain a spherical cap with a decreasing contact angle [24]. At the starting point, $\tilde{t} = 0$, the particles are uniformly distributed inside the domain with a global volumetric concentration, ϕ. Afterward, on each Monte Carlo step (MCS) of the simulation, each particle can perform a random move with a biased probability distribution into a vacant cell within the domain. The probability is defined by seven components, which are recalculated for each particle on each MCS,

$$p_{\text{move}} = \{p_{x_+}, p_{x_-}, p_{y_+}, p_{y_-}, p_{z_+}, p_{z_-}, p_w\}, \tag{1}$$

where the subscripts x, y, and z indicate the three Cartesian axes, "+" and "−" signs indicate whether this direction matches the direction of the velocity projection on this axis or is the opposite, and p_w is the probability of the "waiting" move. Once p_{move} is determined, the direction of the current move is sampled from the biased distribution. The dimensionless velocity components are considered in each of the probabilities in the directions of x, y, and z.

$$\begin{aligned}
p_{x_-} &= \frac{1}{6\tilde{v}_{\max}} - \frac{\tilde{v}_x}{6\tilde{v}_{\max}^2},\\
p_{x_+} &= \frac{1}{6\tilde{v}_{\max}} - \frac{\tilde{v}_x}{6\tilde{v}_{\max}^2} + \frac{\tilde{v}_x}{3\tilde{v}_{\max}},\\
p_{y_-} &= \frac{1}{6\tilde{v}_{\max}} - \frac{\tilde{v}_y}{6\tilde{v}_{\max}^2},\\
p_{y_+} &= \frac{1}{6\tilde{v}_{\max}} - \frac{\tilde{v}_y}{6\tilde{v}_{\max}^2} + \frac{\tilde{v}_y}{3\tilde{v}_{\max}},\\
p_{z_-} &= \frac{1}{6\tilde{v}_{\max}} - \frac{\tilde{v}_z}{6\tilde{v}_{\max}^2},\\
p_{z_+} &= \frac{1}{6\tilde{v}_{\max}} - \frac{\tilde{v}_z}{6\tilde{v}_{\max}^2} + \frac{\tilde{v}_z}{3\tilde{v}_{\max}},\\
p_w &= 1 - p_{x_-} - p_{x_+} - p_{y_-} - p_{y_+} - p_{z_-} - p_{z_+},
\end{aligned} \tag{2}$$

where $\tilde{v}_{\max}$ is calculated as the maximum value from $\max(\tilde{v}_x, \tilde{v}_y, \tilde{v}_z)$ at a given MCS, $\tilde{v}_{\max} > 1$ is the dimensionless velocity of the fastest particle, and $\tilde{v}_x$, $\tilde{v}_y$, and $\tilde{v}_z$ are the dimensionless velocity components, calculated from the analytical solutions for the liquid flow in an evaporating droplet [23,24],

$$\begin{aligned}
\tilde{v}_r(\tilde{r},\tilde{z},\tilde{t}) &= \frac{3}{8(1-\tilde{t})}[(1-\tilde{r}^2) - (1-\tilde{r}^2)^{-\lambda(\theta)}]\left(\frac{\tilde{z}^2}{\tilde{h}^2} - \frac{2\tilde{z}}{\tilde{h}}\right) - \frac{gh_0\tilde{h}}{2R}\left(\frac{\tilde{z}}{\tilde{h}} - \frac{3}{2}\frac{\tilde{z}^2}{\tilde{h}^2}\right),\\
\tilde{v}_z(\tilde{r},\tilde{z},\tilde{t}) &= \frac{3}{4(1-\tilde{t})}[1 + \lambda(\theta)(1-\tilde{r}^2)^{-\lambda(\theta)-1}]\left(\frac{\tilde{z}^3}{3\tilde{h}^2} - \frac{\tilde{z}^2}{\tilde{h}}\right) + \frac{3}{2}\frac{1}{1-\tilde{t}}[(1-\tilde{r}^2) - (1-\tilde{r}^2)^{-\lambda(\theta)}]\\
&\quad\times\left(\frac{\tilde{z}^2}{2\tilde{h}^2} - -\frac{\tilde{z}^3}{3\tilde{h}^3}\right)\tilde{h}(0,\tilde{t}) + \frac{gh_0}{4\tilde{r}}\left(\tilde{z}^2 - \frac{\tilde{z}^3}{\tilde{h}}\right) + \frac{g'h_0}{4}\left(\tilde{z}^2 - \frac{\tilde{z}^3}{\tilde{h}}\right) - \frac{g'h_0\tilde{r}}{2}\frac{\tilde{z}^3}{\tilde{h}^2}\tilde{h}(0,\tilde{t}),\\
g(\tilde{r},\tilde{t}) &= -2h_0\tilde{r}[\tilde{J}(\theta)\lambda(\theta)(1-\tilde{r}^2)^{-\lambda(\theta)-1} + 1] - f(\text{Ma},\Delta T,\nu),
\end{aligned} \tag{3}$$

where the nondimensional instantaneous variables are defined as radial velocity, $\tilde{v}_r = v_r t_f/R$; vertical velocity, $\tilde{v}_z = v_z t_f/R$; time, $\tilde{t} = t/t_f$; radial coordinate, $\tilde{r} = r/R$; vertical coordinate, $\tilde{z} = z/h_0$; and liquid layer thickness, $\tilde{h} = h/h_0$; in which t_f is the total drying time, R is the droplet base radius, and h_0 is the maximum initial droplet height; $\lambda(\theta)$ is linearly dependent on the current contact angle value θ, with the expression $\lambda(\theta) = 1/2 - \theta/\pi$; g' is the first-order partial derivative of the function $g(\tilde{r},\tilde{t})$, with $\tilde{r}$; $\tilde{J} = \tilde{J}(0,\tilde{t})$ is the dimensionless evaporative flux at the top of the droplet surface, and proportional to $(0.27\theta^2 + 1.3)[0.6381 - 0.2239(\theta - \frac{\pi}{4})^2]$, according to Hu and Larsson [24]; and $f(\text{Ma},\Delta T,\nu)$ is a Marangoni effect function of the cumulative influence of the temperature and surfactant gradients. Based on the study [19], our simulations showed that the low dimensionless values of f ($f < 15$) did not significantly affect the final structures, therefore the f term is set to a constant low value ($f = 10$) for all the runs in the present simulation. The expressions of $\tilde{v}_r$ and $\tilde{v}_z$ are calculated for each particle and recalculated for each MCS, then the horizontal velocity components in the x and y directions are simply derived from projections $v_x = v_r x/r$ and $v_y = v_r y/r$. Particles reaching the domain boundary or the coffee ring are excluded from this calculation, since their actual velocity is 0.

Importantly, the model considers the possible particle agglomeration into clusters on each MCS by implementing the DLCA algorithm [8,28]. A sticking parameter, $p_{\text{stick}} > 0$, is applied to control the probability of the particle sticking. The aggregation event is a binary random variable sampled for the particles occupying the nearest neighboring cells. The probability of success is equal to $p_{\text{stick}}\Delta\tilde{t}$, where p_{stick}

is fixed during the run, and $\Delta\tilde{t}$ is the duration of current MCS: $\Delta\tilde{t} = 2/(3B\tilde{v}_{\max})$, in which B is the number of cells in the lattice diameter (1000–3000 in the present work). If the sampled variable is 1 (true), the aggregation occurs, and on the next MCS the aggregated particles move together as a whole cluster.

Three informal sticking ranges may empirically be established for convenience and related to the particle agglomeration rate: weak agglomeration ($0 < p_{\text{stick}} < 1$), moderate agglomeration ($1 < p_{\text{stick}} < 10$), and strong agglomeration ($p_{\text{stick}} > 10$). The performed simulation runs primarily focused on the strong connection between the particle agglomeration rate and the morphology of the fully dried particle structures left on the substrate. The significant influences of particle concentration, initial contact angle, and domain size were investigated as well. Several model assumptions, such as the linear decrease of the droplet height over time and the particle agglomeration hypothesis, have been verified by the experiments.

III. EXPERIMENTS

In the preparation of nanofluids, we used deionized water with the resistivity of 18.0 MΩ cm as the base fluid. The 25 nm aluminum oxide nanoparticles (Nanostructured and Amorphous Materials, Inc.) were mixed in the water with mass concentration of 0.1, 0.2, and 0.5%. The mass preparation was carried out by using a sensitive mass balance with an accuracy of 0.1 mg. The 0.1% CTAB from Sigma Inc. in weight as the surfactant was added in some nanofluid samples but not in the other samples to modify the sticking coefficient among the particles. The CTAB surfactant was managed to reduce the agglomeration of nanoparticles [8]. The cationic dispersant is considered to decrease the particle sticking probability, while the particles in nanofluids free of surfactant are considered to have a higher sticking probability. Then the prepared nanofluids were stirred before they were maintained in an ultrasonication bath (Fisher Scientific Model 500) for more than 2 h to ensure the even dispersion of the nanoparticles in the base fluids initially. The brand new and clean silicon wafers (Latech Scientific Supply Pte. Ltd.) were used as the substrates for nanofluid droplet drying. Right after the suspensions were made, tiny sessile droplets, 0.99 ± 0.15 mm in diameter, were placed on the substrate through an accurate pipette. We used the tensiometer (Theta Optical Tensiometer, LTD2) to measure the maximum height of the sessile nanofluid droplet as a function of time in the drying process. The initial contact angle of the sessile evaporating droplets was about 30° from the side-view camera. The droplets were dried in open conditions at 25 °C room temperature, 1 atm ambient pressure, and 40% relative humidity. The morphology of drying structures was measured under an optical microscope from the top view (LV100D-U from Nikon Inc.).

IV. RESULTS AND DISCUSSION

Figure 2 illustrates the results of a single simulation run leading to the formation of a coffee-ring structure. The droplet base diameter is set to 1000 cells; the initial contact angle θ_0 is assumed to be 30°, based on the experimental observation shown in the later section; and the nondimensional single-particle size is one cell with the dimension of $1 \times 1 \times 1$. The simulation starts at $\tilde{t} = 0$ with all the particles uniformly distributed inside a pinned sessile droplet [see Fig. 2(a)]. As the simulation progresses, the droplet starts to shrink in the vertical direction but with a constant contact radius, and the replenishing capillary flow [3,5] brings particles toward the three-phase contact line, as Figs. 2(b)–2(f) display. During the second half of the droplet lifetime more particles arrive to the edge contributing to the continuous growth of the ring width [Figs. 2(g)–2(k)]. At the latest drying stage, corresponding to Figs. 2(l)–2(r), the capillary flow velocity

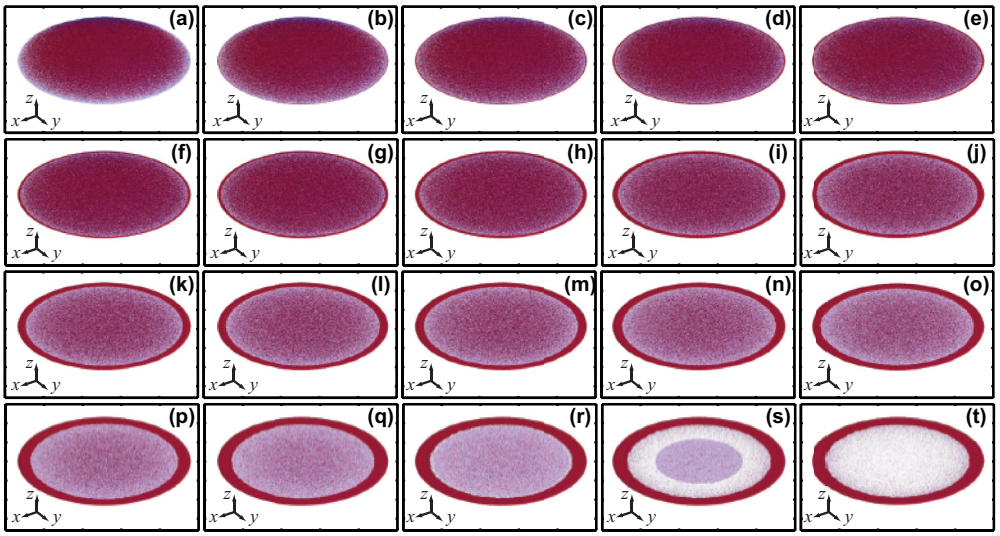

FIG. 2. (Color online) Progression of the coffee-ring formation during the droplet drying process over time in a single Monte Carlo simulation run. (a) Initial system state at $\tilde{t} = 0$ from the isometric view. (b)–(t) Corresponding images of the drying droplet after time elapsed: (b) $\tilde{t} = 0.1$, (c) $\tilde{t} = 0.2$, (d) $\tilde{t} = 0.3$, (e) $\tilde{t} = 0.4$, (f) $\tilde{t} = 0.5$, (g) $\tilde{t} = 0.6$, (h) $\tilde{t} = 0.7$, (i) $\tilde{t} = 0.8$, (j) $\tilde{t} = 0.85$, (k) $\tilde{t} = 0.9$, (l) $\tilde{t} = 0.91$, (m) $\tilde{t} = 0.92$, (n) $\tilde{t} = 0.93$, (o) $\tilde{t} = 0.94$, (p) $\tilde{t} = 0.96$, (q) $\tilde{t} = 0.97$, (r) $\tilde{t} = 0.98$, (s) $\tilde{t} = 0.99$, (t) $\tilde{t} = 1$. Parameters: $p_{\text{stick}} = 0.01$, $\phi = 1\%$, $\theta_0 = 30°$. The domain base diameter is 1000 cells. The full animation is available as the Supplementary Video-1 [30].

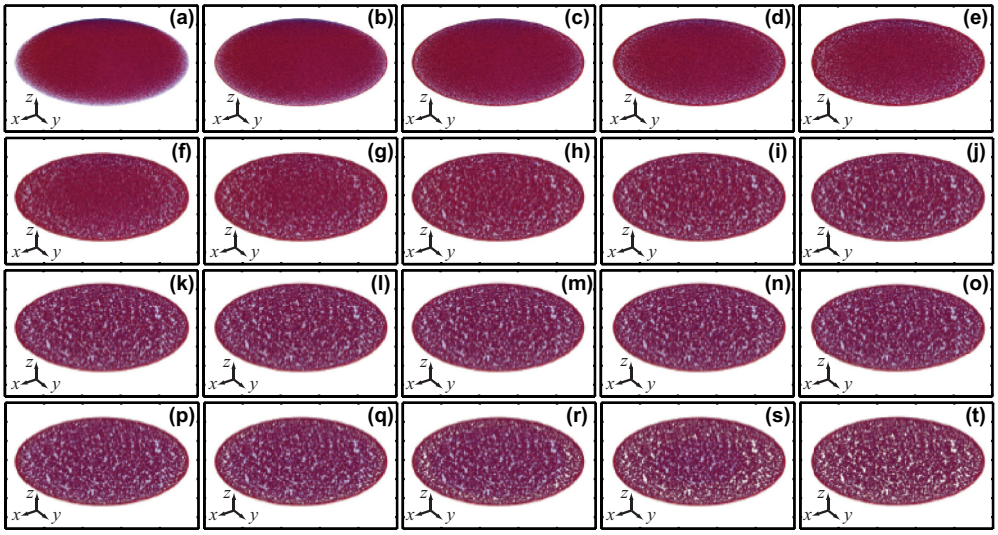

FIG. 3. (Color online) Progression of the uniform film formation over time in a single Monte Carlo simulation run from the isometric view. (a) $\tilde{t} = 0$, (b) $\tilde{t} = 0.1$, (c) $\tilde{t} = 0.2$, (d) $\tilde{t} = 0.3$, (e) $\tilde{t} = 0.4$, (f) $\tilde{t} = 0.5$, (g) $\tilde{t} = 0.6$, (h) $\tilde{t} = 0.7$, (i) $\tilde{t} = 0.8$, (j) $\tilde{t} = 0.85$, (k) $\tilde{t} = 0.9$, (l) $\tilde{t} = 0.91$, (m) $\tilde{t} = 0.92$, (n) $\tilde{t} = 0.93$, (o) $\tilde{t} = 0.94$, (p) $\tilde{t} = 0.96$, (q) $\tilde{t} = 0.97$, (r) $\tilde{t} = 0.98$, (s) $\tilde{t} = 0.99$, (t) $\tilde{t} = 1$. Parameters: $p_{\text{stick}} = 25$, $\phi = 2\%$, $\theta_0 = 30^\circ$. The domain base diameter is 1000 cells. The full animation is available as the Supplementary Video-2 [30].

increases significantly, and most of the remaining single particles are wiped off the substrate inside the ring toward the rim. Finally, the remaining thin layer of liquid dries out completely, and the coffee-ring structure is fully formed [see Fig. 2(t)].

Figure 3 presents another drying scenario featuring the process of the uniform film formation. The sticking coefficient is significantly increased from 0.01 to 25, and the particle coverage is now at 2%. All the other model parameters, domain geometry, and particle laws of motion remain the same. The earliest stage of the process looks quite similar to the coffee-ring scenario, starting from a deposition of a thin layer of particles near the three-phase line [Figs. 3(a)–3(c)]. However, the subsequent events are completely different. Particle aggregation in the liquid bulk causes the formation of clusters which start to flow toward the edge. The shape of smaller clusters might resemble the blocks from the popular Tetris game, which are also allowed to agglomerate into larger clusters in our model. As these clusters start to reach the boundary, they rapidly build up a sparse structure spanning from the contact line inward, reaching the center of symmetry and covering the whole substrate, as shown in Figs. 3(d)–3(j). This growth process recalls the losing scenario in the Tetris game, where the randomly arriving blocks are dropped by a player purely at random, thus leaving large gaps inside the structure and eventually overfilling the available space. Oppositely, in the coffee-ring case, the almost regularly shaped blocks uniformly arrive to the boundary, filling in the gaps and forming a densely packed structure (see Fig. 2). The idea for this mechanism was first expressed by Yunker *et al.* and analyzed for a local one-dimensional (1D) case [12]. In the present work the effect is extended and generalized for a full 3D droplet-shaped domain, where the particle moves obey the rules derived from the analytical equations [24], and the cluster aggregation is allowed as well.

Furthermore, a rigorous parameter study is performed investigating the coupled influence of three parameters: p_{stick}, ϕ, and θ_0. Figure 4 presents the final results in the form of a block matrix: each of six numbered blocks corresponds to one sticking value; and inside of each block the two other parameters get three different values, totally producing nine images, labeled with (a)–(i), in each block. The diagram provides a general perspective of the parameter dependencies. Block-by-block comparisons show that the coffee-ring patterns are prevalent for the low sticking range [see Figs. 4(a1)–4(i1) and 4(a2)–4(i2)], the mixed patterns are typical for the moderate agglomeration [see Figs. 4(a3)–4(i3) and 4(a4)–4(i4)], and the uniform pattern is dominating in the strong agglomeration, as seen in Figs. 4(a5)–4(i5) and 4(a6)–4(i6). However, picking any particular block [for example, Figs. 4(a5)–4(i5)] for analysis emphasizes the importance of contact angle and particle concentration as well. The following results display the dependence on each particular parameter in more detail.

Figure 5 shows the dependence on p_{stick} in the cases of particle concentration at $\phi = 2\%$ [Figs. 5(a)–5(f)]. A clear crossover is found from the coffee-ring pattern [Fig. 5(a) toward a uniform film deposit [Fig. 5(f1)]. Figure 5(g) demonstrates the nondimensional local deposition height, H/R, as a function of the scaled radial distance from the domain center, r/R ($\leqslant 1$). The local height H is an average value of the heights at the circle with a radius of r. As p_{stick} increases, the height close to the periphery decreases while the height at the center increases slightly. The relative heights for Fig. 5(a) are distinctly nonuniform, but they are quite uniform for Fig. 5(f). Interestingly, these findings agree well with the previous results for a 2D model on a planar circular domain with significantly simplified conditions [7,8], where the velocity distribution profile followed either a linear law [7] or a simple power-law distribution [8]. The results also indicate that global particle concentration ϕ defines both the ring width and the covered area of a uniform deposit.

Figure 6 provides the visual trends for the dependencies on ϕ in three scenarios: weak [Figs. 6(a)–6(c)], moderate [Figs. 6(d)–6(f)], and strong agglomeration [Figs. 6(g)–6(i)].

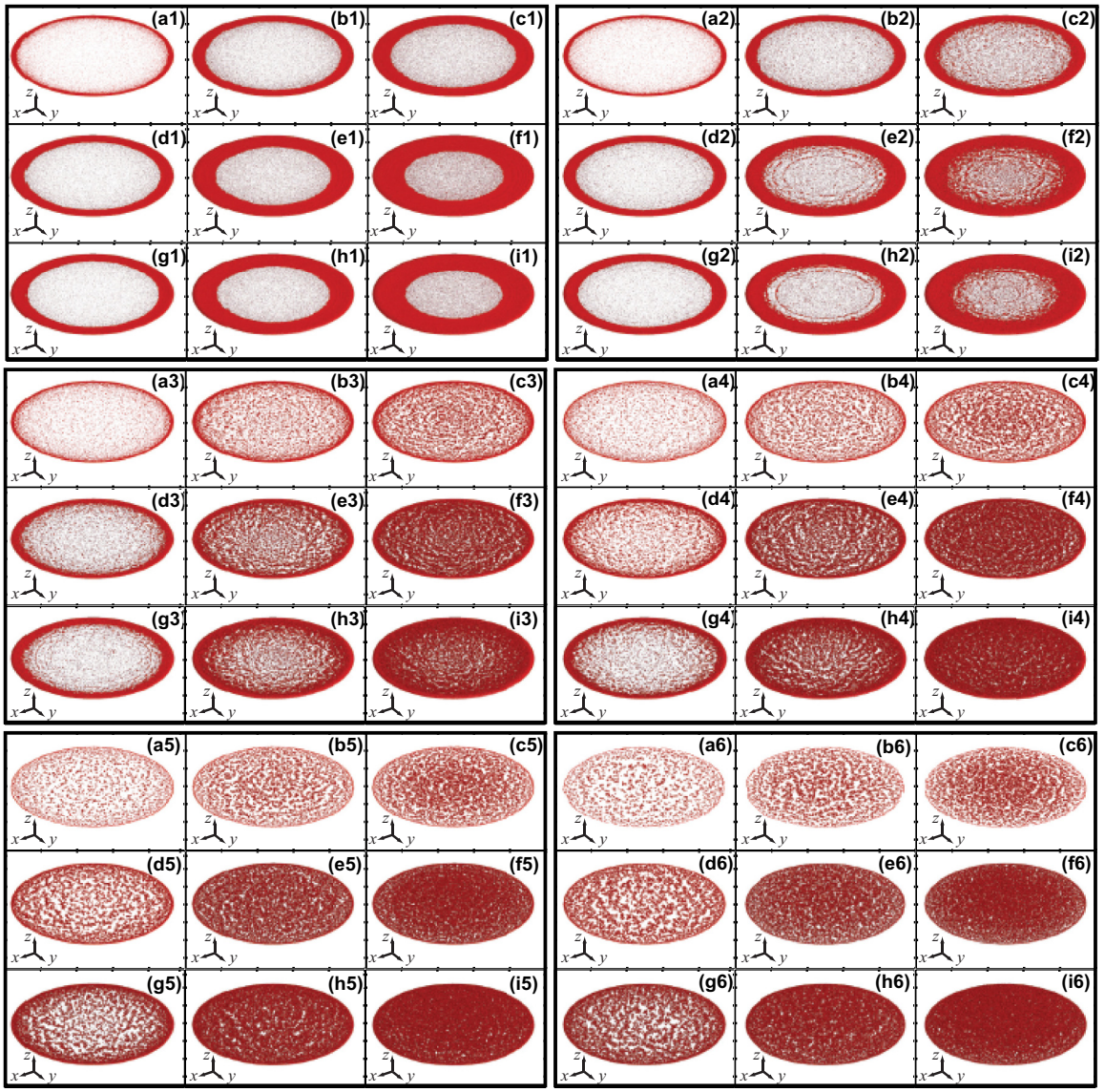

FIG. 4. (Color online) Results of the parameter study, showing the finally dried particle structures. The results in blocks (a1)–(i1) have $p_{\text{stick}} = 0.01$, (a2)–(i2) $p_{\text{stick}} = 1$, (a3)–(i3) $p_{\text{stick}} = 5$, (a4)–(i4) $p_{\text{stick}} = 10$, (a5)–(i5) $p_{\text{stick}} = 25$, and (a6)–(i6) $p_{\text{stick}} = 50$. The 1st and 4th columns have concentrations at $\phi = 1\%$, the 2nd and 5th columns have $\phi = 2\%$, and the 3rd and 6th columns have $\phi = 3\%$. The 1st, 4th, and 7th rows have the initial contact angle $\theta_0 = 10^\circ$, the 2nd, 5th, and 8th rows have $\theta_0 = 30^\circ$, and the 3rd, 6th, and 9th rows have $\theta_0 = 45^\circ$. The domain base diameter is 1000 cells.

The scenario with weak agglomeration at $p_{\text{stick}} = 0.01$ generates the typical coffee-ring pattern, the width of which markedly depends on ϕ. The dependency of the coffee-ring shape on ϕ has been investigated in detail in the previous work [19]. The second scenario with the moderate agglomeration at $p_{\text{stick}} = 5$ is of particular significance here, since it clearly shows how the changing of ϕ alone can qualitatively alter the pattern type [see Figs. 6(d)–6(f)]. The pattern corresponding to the lowest ϕ still mostly resembles the coffee ring [Fig. 6(d)] but the three-fold increase in ϕ produces a mixed result with a fine domain coverage, while the boundary ring is still evident [Fig. 6(f)]. It is the pattern that was also observed in previous experiments but could not be fully explained by means of 2D modeling alone [8]. Finally, the strong-agglomeration scenario is associated with a more uniform domain coverage bounded by a thin ring at the periphery [Figs. 6(g)–6(i)]. The local height of the formed patterns can be seen in Fig. 6(j) for the switch from the coffee ring to the uniform deposition as a function of volumetric particle concentration. The overall conclusion for the last two scenarios is that adding more particles into the system does not change the boundary ring size and structure, but increases the area of the clusters covering the substrate inside the domain.

This part of the specific parameter analysis focuses on the effect of initial droplet contact angle θ_0, with the results summarized in Fig. 7. The three scenarios of weak [Figs. 7(a)–7(c)], moderate [Figs. 7(d)–7(f)], and strong agglomeration [Figs. 7(g)–7(i)] are considered again. Changing the angle from 10° to 30° produces different results from increasing it further from 30° up to 45°. Increasing θ_0 from a small value

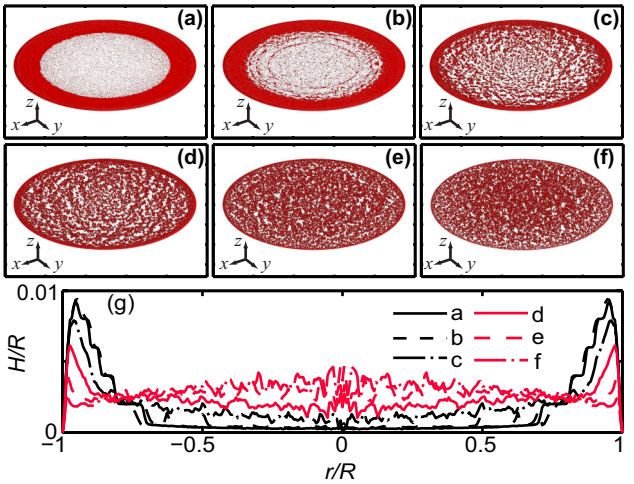

FIG. 5. (Color online) The simulation results focusing on the dependence of the dried-in patterns on the sticking parameter, p_{stick}. The images in series have the concentration value at $\phi = 2\%$, the initial contact angle, $\theta_0 = 30^\circ$, and correspond to the sticking values at: (a) $p_{\text{stick}} = 0.01$, (b) $p_{\text{stick}} = 1$, (c) $p_{\text{stick}} = 5$, (d) $p_{\text{stick}} = 10$, (e) $p_{\text{stick}} = 25$, (f) $p_{\text{stick}} = 50$. (g) The diagram displays the dependence of the averaged structure height profile on the radial distance from the domain center. Each curve corresponds to a certain p_{stick} value, and the averaged particle layer height is scaled by the domain radius. The domain base diameter is 1000 cells ($R = 500$).

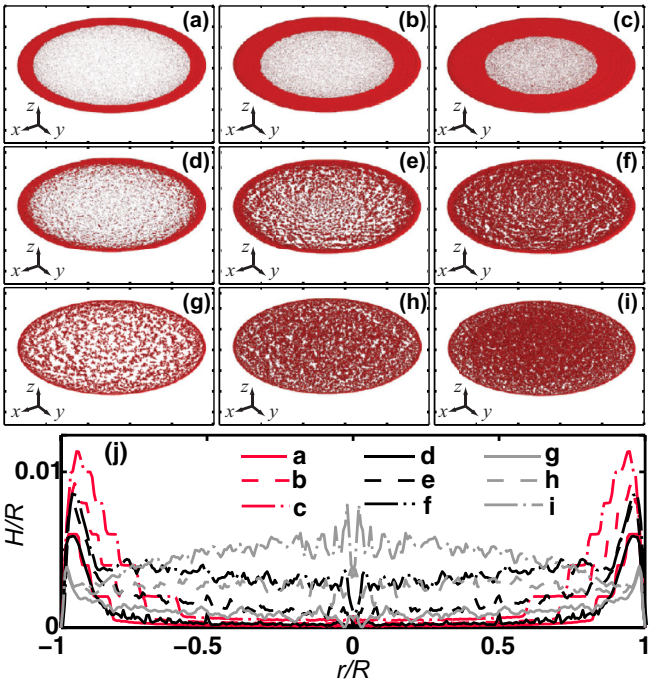

FIG. 6. (Color online) Final simulation results for the initial contact angle, $\theta_0 = 30^\circ$, and illustrating the dependence on the volumetric particle concentration ϕ. (a)–(c) Coffee-ring configuration: $p_{\text{stick}} = 0.01$; (d)–(f) transient configuration: $p_{\text{stick}} = 5$; and (g)–(i) uniform configuration: $p_{\text{stick}} = 25$. Concentration values: (a), (d), (g) $\phi = 1\%$; (b), (e), (h) $\phi = 2\%$; (c), (f), (i) $\phi = 3\%$. (j) Dependence of the averaged structure height profile on the radial distance from the domain center for each result. The domain base diameter is 1000 cells ($R = 500$).

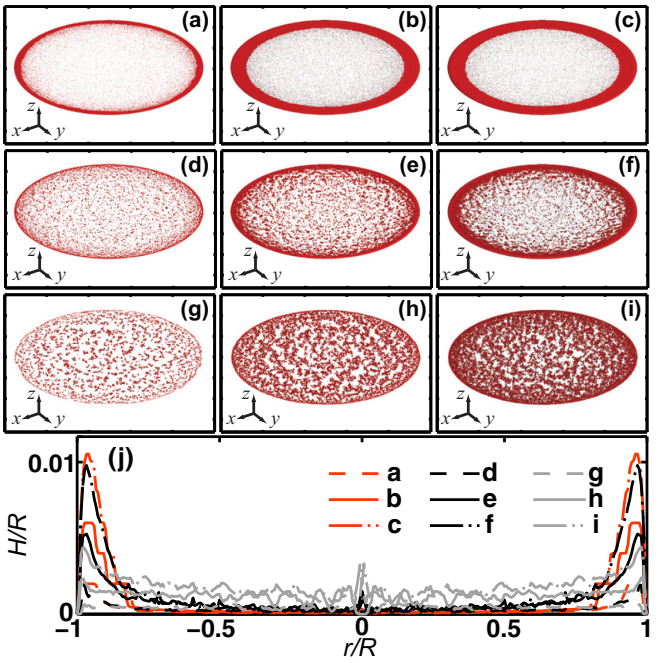

FIG. 7. (Color online) Simulation results focusing on the dependence on the initial droplet contact angle value θ_0. (a)–(c) Coffee-ring configuration: $p_{\text{stick}} = 0.01$; (d)–(f) transient configuration: $p_{\text{stick}} = 10$; (g)–(i) uniform configuration: $p_{\text{stick}} = 50$. Contact angle values: (a), (d), (g) $\theta_0 = 10^\circ$; (b), (e), (h) $\theta_0 = 30^\circ$; and (c), (f), (i) $\theta_0 = 45^\circ$. (j) Dependence of the averaged structure height profile on the radial distance from the domain center for each result. The domain base diameter is 1000 cells ($R = 500$), and $\phi = 1\%$.

of 10° affects both the ring width [compare Figs. 7(a) and 7(b)] and the particle presence in the inner area [compare Figs. 7(g) and 7(h)], for all scenarios. However, increasing the angle further does not lead to any significant changes in the inner area; the additional particles, coming from the increased overall droplet volume, contribute only to the ring thickness [height in the 3D patterns shown in Fig. 7(j)] and the area next to periphery [see Figs. 7(e) and 7(f), for example].

An additional quick study explains the effect of an increase in the possible domain diameter from 1000 cells up to 3000 cells in the coffee-ring case (see Fig. 8). The results clearly demonstrate that larger domains produce more prominent

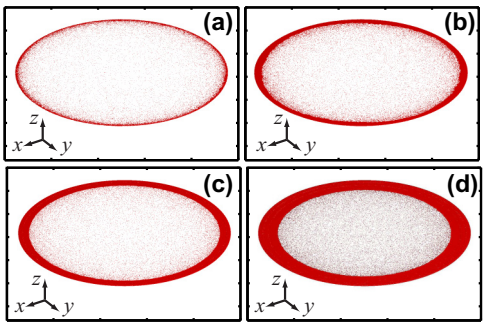

FIG. 8. (Color online) Results of investigating the dependence of the coffee-ring structure on the simulation domain size. (a)–(b) 1000 base diameter; (c)–(d) 3000 base diameter. Concentration values: (a), (c) $\phi = 0.5\%$; (b), (d) $\phi = 1\%$. All have $\theta_0 = 30^\circ$.

and well-shaped rings, shown in Figs. 8(c) and 8(d). This finding thus leads to two suggestions: (i) larger size droplets can produce wider and more pronounced rings, and (ii) simulations in larger domains would require lower particle concentrations to produce the similar structures. Suggestion (i) can be the subject of an interesting experimental investigation; however, it might be difficult to keep the other parameters, such as the apparent contact angle, unchanged if the droplet volume is increased on the ground experiments. Suggestion (ii) can explain a much lower particle concentration used in our experiments, which is of the order of 0.1–0.5% in the present work, as well as our previous works on the topic [7,8], and 0.1% used by Dugyala and Basavaraj [11] in their recent work on ellipsoidal particles. For a typical 1–3 mm (in base diameter) sessile droplet and 5–100 nm particles, the corresponding domain size would be in 10 000–600 000 range, which is difficult to achieve by means of present common computational tools but might evidently produce more accurate estimation. However, we suggest here that basic trend estimations and comparisons may be performed in a 3D domain with 1000 cells as the base diameter, while keeping in mind a necessity to put higher concentrations of particles into the simulated system.

Two hypotheses used in the modeling have been verified by the experimental observations first, in order to prove the validity of the model. The time evolution of the experimental agglomeration process is included in Fig. 9, captured with the optical microscope. The process looks general and not limited only to the free surface of the droplet. Also, there was no excessive adsorption detected on the interface in the conditions with no surfactant added and when the aggregation process is the strongest. This fact provides the idea to not limit the particle aggregation process to only the droplet interface in the simulation and to consider possible aggregation events in the liquid volume as well.

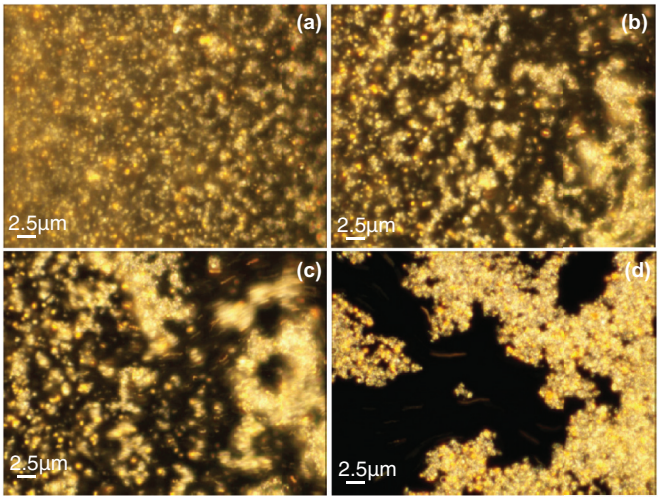

FIG. 9. (Color online) Captured sequence of images illustrating the alumina particle agglomeration process in liquid. The dark field mode of the optical microscope was used. Particles are in bright colors, the substrate is black. Small clusters located in different layers of the droplet have progressively aggregated into a large supercluster blocking the outward flow.

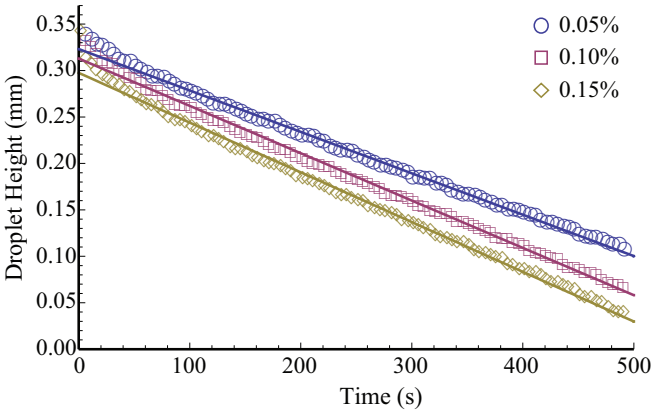

FIG. 10. (Color online) Recorded dependence of the nanofluid sessile droplet maximum height on evaporation time, shown for three different droplets. The dependence is visibly close to the linear law for most of the process except for a very initial time period. Straight fitting lines are added for visual comparison of the actual trends and the linear law.

The decrease of the drying nanofluid droplet maximum height over time was experimentally observed to produce similar results in the nanofluids with different particle concentrations. The examples of 0.05%, 0.10%, and 0.15% nanofluids are shown in Fig. 10. From the direct measurements, the dependence is roughly linear for the most of the drying time suggesting that it is worthwhile to consider a linear law in the model.

We also performed a series of qualitative comparisons between the simulated and experimental results from dying the alumina nanofluid droplet in open conditions, similar to previous works [7,8]. The results are grouped into a diagram in Fig. 11 for comparison. The experimental results shown in Figs. 11(a1), 11(a2), 11(b1), 11(b2), 11(c1), and 11(c2) illustrate the possible coffee-ring patterns under different combinations of experimental parameters: particle mass concentration c_{part} and the CTAB surfactant mass concentration c_{surf}. We include two images for most of the experimental samples to demonstrate the repeatability of the produced results. In reality, more than 10 tiny droplets were used for each of the sampled nanofluids producing similar patterns. The corresponding simulation results in Figs. 11(a3)–11(c3) qualitatively show the best-matching coffee-ring patterns. More rigorous comparison could be suggested for future work, since it has not yet been investigated in detail how the surfactant and particle concentrations affect the droplet contact angle, particle agglomeration rate, and other parameters. However, the overall agreement between the results is present, since higher particle concentrations produce wider rings in the images of columns (a)–(c) in Fig. 11. In general, the CTAB surfactant use in the experiments corresponds to the weak agglomeration scenarios in the simulations—the phenomena discussed in the previous works for 2D models [7,8].

Moreover, the most striking outcome of the comparison is seen in the last two columns of Figs. 11(d) and 11(e). Being also confirmed previously [8], the samples entirely without surfactant produce a sparsely looking uniform domain coverage, surrounded by a thin boundary ring [see Figs. 11(d1)

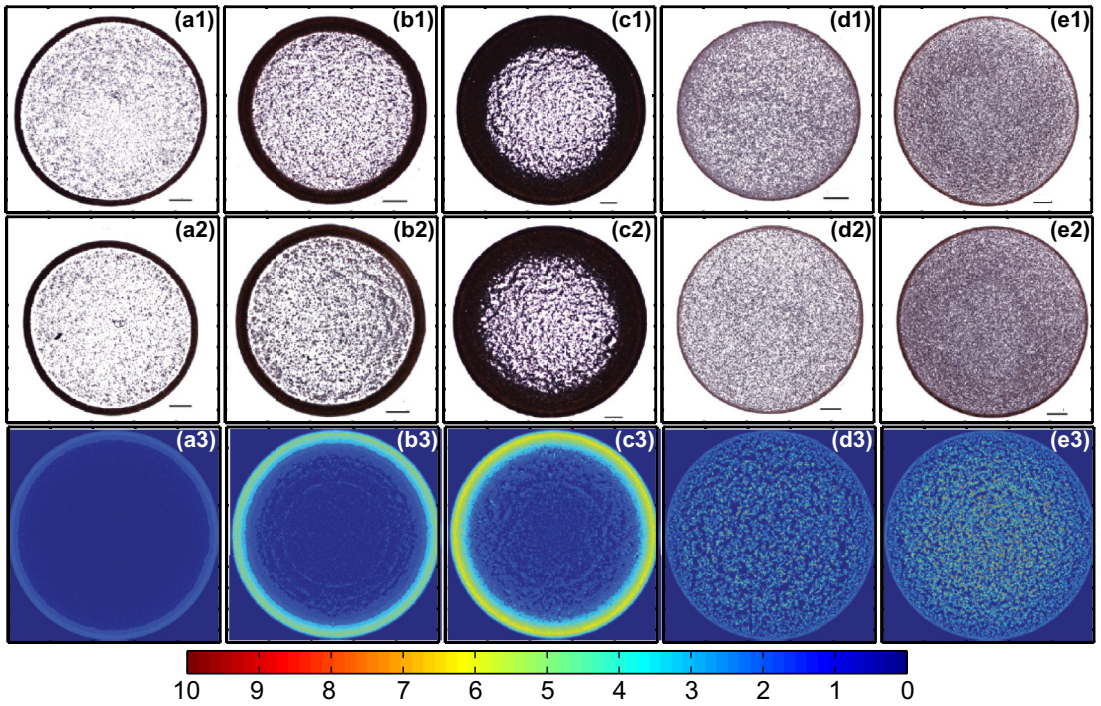

FIG. 11. (Color online) Comparison between the simulated and experimental results. Experimental conditions: (a1) $c_{\text{part}} = 0.1\%$, $c_{\text{surf}} = 0.01\%$; (a2) $c_{\text{part}} = 0.2\%$, $c_{\text{surf}} = 0.01\%$; (b1),(b2) $c_{\text{part}} = 0.5\%$, $c_{\text{surf}} = 0.01\%$; (c1),(c2) $c_{\text{part}} = 0.5\%$, $c_{\text{surf}} = 0.1\%$; (d1),(d2) $c_{\text{part}} = 0.1\%$, $c_{\text{surf}} = 0\%$; (e1),(e2) $c_{\text{part}} = 0.2\%$, $c_{\text{surf}} = 0\%$. The scale is 100 μm for all the experimental images. The 2D color maps indicate the thickness of the particle layer in the 3D simulated structure. (a3)–(e3) The simulation results with the corresponding parameter values: (a3) $\phi = 0.5\%$, $\theta_0 = 30^\circ$, $p_{\text{stick}} = 0.5$; (b3) $\phi = 2\%$, $\theta_0 = 30^\circ$, $p_{\text{stick}} = 1$; (c3) $\phi = 3\%$, $\theta_0 = 30^\circ$, $p_{\text{stick}} = 1$; (d3) $\phi = 2\%$, $\theta_0 = 30^\circ$, $p_{\text{stick}} = 25$; (e3) $\phi = 3\%$, $\theta_0 = 30^\circ$, $p_{\text{stick}} = 25$. The simulation domain base diameter is 1000 cells.

and 11(d2) and Figs. 11(e1) and 11(e2)]. The highly nontrivial change corresponds well to the switch in the simulations from the weak ($0.01 < p_{\text{stick}} < 1$) to the strong agglomeration scenario ($p_{\text{stick}} = 25$), which produces patterns with similar morphology [Figs. 11(d3) and 11(e3)]. Furthermore, increasing particle concentration in the experimental samples produces a higher density coverage of the inner area, shown in Figs. 11(e1) and 11(e2); a similar effect is observed in the simulation with a higher ϕ [Fig. 11(e3)].

V. CONCLUSIONS

A 3D lattice model has been developed to simulate the drying process of a pinned sessile colloidal droplet. The model combines the BRW and DLCA approaches and is based on the analytical expression for liquid flow developed previously. The simulation results provide a view of the crossover from the coffee-ring effect toward the uniform film deposit, and relate the observed phenomenon to the rapid structure buildup in a popular Tetris game. The parameter study results predict the transformational trends in the final structure morphology, extending the previously reported 1D and 2D simulation approaches. The qualitative comparison with the experimental results is performed reproducing the experimental patterns and trends by controlling the model parameters. The limitations of the model include the domain size, which is significantly smaller than the actual droplet size. It means that the number of particles in the simulated droplet is much lower than the true number used in the experiments. However, the domain size study results suggest that the basic analysis may still be performed in a small domain. Other suggestions for future work include a detail study of the experimental parameters and their dependencies, such as particle and surfactant concentrations, diffusion and evaporation rates, particle agglomeration, and contact angle. Additionally, using 3D profilometry is suggested for measurement of the actual coffee-ring profiles of different samples and comparison with the simulated results.

ACKNOWLEDGMENT

F.D. is thankful for support from the Ministry of Education (MOE) Academic Research Fund (AcRF) Tier 1 RG120/14.

[1] H. Y. Erbil, Adv. Colloid Interface Sci. **222**, 275 (2015).
[2] X. Zhong, A. Crivoi, and F. Duan, Adv. Colloid Interface Sci. **217**, 13 (2015).
[3] R. D. Deegan, O. Bakajin, T. F. Dupont, G. Huber, S. R. Nagel, and T. A. Witten, Nature **389**, 827 (1997).
[4] R. D. Deegan, O. Bakajin, T. F. Dupont, G. Huber, S. R. Nagel, and T. A. Witten, Phys. Rev. E **62**, 756 (2000).
[5] H. Hu and R. G. Larson, J. Phys. Chem. B **110**, 7090 (2006).
[6] X. Y. Shen, C. M. Ho, and T. S. Wong, J. Phys. Chem. B **114**, 5269 (2010).

[7] A. Crivoi and F. Duan, J. Phys. Chem. B **117**, 5932 (2013).
[8] A. Crivoi and F. Duan, Phys. Rev. E **87**, 042303 (2013).
[9] T. Still, P. J. Yunker, and A. G. Yodh, Langmuir **28**, 4984 (2012).
[10] P. J. Yunker, T. Still, M. A. Lohr, and A. G. Yodh, Nature **476**, 308 (2011).
[11] V. R. Dugyala and M. G. Basavaraj, Langmuir **30**, 8680 (2014).
[12] P. J. Yunker, M. A. Lohr, T. Still, A. Borodin, D. J. Durian, and A. G. Yodh, Phys. Rev. Lett. **110**, 035501 (2013).
[13] M. Nicoli, R. Cuerno, and M. Castro, Phys. Rev. Lett. **111**, 209601 (2013).
[14] P. J. Yunker, M. A. Lohr, T. Still, A. Borodin, D. J. Durian, and A. G. Yodh, Phys. Rev. Lett. **111**, 209602 (2013).
[15] C. S. Dias, N. A. M. Araujo, and M. M. Telo da Gama, Europhys. Lett. **107**, 56002 (2014).
[16] A. Crivoi and F. Duan, Langmuir **29**, 12067 (2013).
[17] N. I. Lebovka, S. Khrapatiy, R. Melnyk, and M. Vygornitskii, Phys. Rev. E **89**, 052307 (2014).
[18] T. Breinlinger and T. Kraft, Powder Technol. **256**, 279 (2014).
[19] A. Crivoi and F. Duan, Sci. Rep. **4**, 4310 (2014).
[20] D. Huang, L. Ma, and X. Xu, Int. J. Heat Mass Transfer **83**, 307 (2015).
[21] M. Kolb and H. J. Herrmann, Phys. Rev. Lett. **59**, 454 (1987).
[22] J. Vermant, Nature **476**, 286 (2011).
[23] H. Hu and R. G. Larson, Langmuir **21**, 3972 (2005).
[24] H. Hu and R. G. Larson, Langmuir **21**, 3963 (2005).
[25] E. A. Codling, M. J. Plank, and S. Benhamou, J. R. Soc. Interface **5**, 813 (2008).
[26] M. G. Gauthier and G. W. Slater, Physica A **355**, 283 (2005).
[27] M. G. Gauthier and G. W. Slater, Phys. Rev. E **70**, 015103 (2004).
[28] P. Meakin, *Fractals, Scaling and Growth Far from Equilibrium* (Cambridge University, Cambridge, England, 1998).
[29] A. Hasmy and R. Jullien, Phys. Rev. E **53**, 1789 (1996).
[30] See Supplemental Material at http://link.aps.org/supplemental/10.1103/PhysRevE.92.032302 for the corresponding movies.